Three-Dimensional Structure of Toxin OSK1 from *Orthochirus scrobiculosus* Scorpion Venom[†,‡]

Victor A. Jaravine, Dmitry E. Nolde, Michail J. Reibarkh, Yulia V. Korolkova, Sergey A. Kozlov,
Kirill A. Pluzhnikov, Eugene V. Grishin, and Alexander S. Arseniev*

Shemyakin and Ovchinnikov Institute of Bioorganic Chemistry, Russian Academy of Sciences, Ul. Miklukho-Maklaya 16/10, Moscow 117871, Russia

Received June 17, 1996; Revised Manuscript Received September 3, 1996[⊗]

ABSTRACT: A 600 MHz ^{1}H NMR study of toxin OSK1, blocker of small-conductance Ca^{2+}-activated K^+ channels, is presented. The unambiguous sequential assignment of all the protons of the toxin was obtained using TOCSY, DQF-COSY, and NOESY experiments at pH 3.0 (10, 30, and 45 °C) in aqueous solution. $^3J_{N\alpha}$, $^3J_{\alpha\beta}$ vicinal spin coupling constants were determined in high-resolution spectra. The cross-peak volumes in NOESY spectra and the coupling constants were used to define the local structure of the protein by the program HABAS and to generate torsion angle and interproton distance constraints for the program DIANA. Hydrogen−deuterium exchange rates of amide protons showed possible locations of hydrogen bonds. The hydrogen bond acceptors and disulfide bridges between residues 8−28, 14−33, and 18−35 were determined when analyzing distance distribution in preliminary DIANA structures. All constraints were used to obtain a set of 30 structures by DIANA. The resulting rms deviations over 30 structures are 1.30 Å for the heavy atoms and 0.42 Å for the backbone heavy atoms. The structures were refined by constrained energy minimization using the SYBYL program. Their analysis indicated the existence of the α-helix (residues 10−21) slightly distorted at the Cys14 residue, two main strands of the antiparallel β-sheet (24−29, 32−38), and the extended fragment (2−6). The motif is stabilized by the disulfide bridges in the way, common to all known scorpion toxins. Using the fine spatial toxin structure, alignment of the homologues, mutagenesis analysis, and comparison of scorpion toxin family functions, we delineate some differences significant for the toxin specificity.

Natural venoms are a rich source of molecules interacting with different membrane receptors and ionic channels. These agents perturb normal functioning of an organism, thus being efficient to subdue prey. Some of the short scorpion toxins have been studied with respect to their structure, biochemical interaction, or functional specificity. These include charybdotoxin (ChTX)[1] (Bontems et al., 1992), iberiotoxin (IbTX) (Johnson & Sugg, 1992), PO5-NH_2 (Meuner et al., 1993), kaliotoxin (KTX) (Fernandez et al.,1994), margatoxin (MgTX) (Johnson et al., 1994), noxiustoxin (NTX) (Dauplas et al., 1996), and agiotoxin (AgTX) (Kreizel et al., 1995). All of the short scorpion toxins have similar function and the same α/β structural motif. The toxins are small in size, accessible to chemical synthesis, highly stable, and tolerant of sequence mutations. Antibacterial insect defensins adopt a folding pattern very similar to one of the scorpion toxins (Bontems et al., 1991). This motif served as a basic for protein engineering, where a metal binding site was introduced into the β-sheet (Vita et al., 1995). However, very little is known about the structural basis of different types of the toxin functionality.

OSK1, novel scorpion toxin, is a single-chain, highly positively charged (7 Lys^+, 1 Arg^+, against 1 Glu^- residue) polypeptide consisting of 38 amino acid residues. The toxin blocks apamin-insensitive small-conductance Ca^{2+}-activated K^+ channels in neuroblastoma-glioma NG 108-15 hybrid cells (Grishin et al., 1996). The toxin displays sequence homology to the other known short toxins from different scorpion venoms also targeted toward K^+ channels. There are two main channel types: Ca^{2+}-activated and voltage-dependent K^+ channels. Toxins can usually affect the activity of both the types, but their specificity is different. Data on the toxin affinity to different channels are incomplete, mainly due to diversity of the latter.

OSK1 indicated high homology to the kaliotoxin group: 79% amino acid residues of OSK1 are identical to those of KTX, specifically blocking the intermediate-conductance Ca^{2+}-activated K^+ channels and also binding to the dendrotoxin-sensitive voltage-dependent (Shaker) K^+ channels (Reinhart, 1989). At the same time the highest sequence homology (82%) is observed between OSK1 and AgTX, which is a high-affinity inhibitor of the Shaker channels (Blatz, 1987). OSK1 has 50% homology to the NTX-delayed rectifier voltage-dependent K^+-channel inhibitor slightly effecting Ca^{2+}-activated K^+ channels (Valdivia et al., 1988). MgTX, a 52% homologue, blocks the lymphocyte voltage-dependent channel but is ineffective to the lymphocyte Ca^{2+}-activated K^+ channels (Leonard et al., 1992).

[†] This work was supported by grants from the Russian Basic Research Foundation.

[‡] Atomic coordinates of 30 energy-refined structures have been deposited in the Brookhaven Protein Data Bank under the file name 1SCO.

* To whom correspondence should be addressed.

[⊗] Abstract published in *Advance ACS Abstracts,* November 15, 1996.

[1] Abbreviations: AgTX, agiotoxin; ChTX, charybdotoxin; IbTX, iberiotoxin; KTX, kaliotoxin; MgTX, margatoxin; NTX, noxiustoxin; OSK1, *Orthochirus scrobiculosus* scorpion toxin 1; NMR, nuclear magnetic resonance; DQF-COSY, double-quantum-filtered correlated spectroscopy; TOCSY, total correlated spectroscopy; NOE, nuclear Overhauser effect; NOESY, NOE spectroscopy; rmsd, root mean square deviation; HPLC, high-performance liquid chromatography; PDB, protein data bank; Z, one-letter code for pyroglutamic acid.

S0006-2960(96)01439-0 CCC: $14.00

Lower homology (37%) is found with ChTX, which is highly selective for high-conductance Ca^{2+}-activated K^+ channels but moderately blocking Shaker channels (Vazquez, 1990). The α/β-fold adopted by the scorpion toxins is capable of exerting the functional variability, presumably reflecting the diversity of K^+ channels. However, its structural basis is poorly understood. Therefore, investigation of the toxin spatial structure at the highest resolution seems relevant, thus promoting to clarify the mode of its action and structure−functional differences with regard to other channel-acting toxins.

This paper deals with the complete determination of the OSK1 three-dimensional structure in aqueous solution by a ^1H NMR technique and analysis of the structure−functional relationship within the family of short scorpion toxins accounting for fine details of their spatial structures.

MATERIALS AND METHODS

Sample Preparation. OSK1 was isolated and purified from the venom of the Central Asian scorpion *Orthochirus scrobiculosus*, as described in Grishin et al. (1996). Its molecular mass is 4205.7 Da. According to analytical HPLC the purity of the sample was 97%; mass spectrometry showed the sample to be individual. For the NMR experiments 3.1 mg of the lyophilized protein was dissolved in 150 μL of sodium phosphate buffer (including 10% ^2H_2O as internal lock) to yield a final concentration of 4.9 mM and pH 3.0. The sample was later lyophilized, dissolved in 150 μL of ^2H_2O, and used for measuring exchange rates of amide protons with deuterium. After being measured it was lyophilized again, dissolved in 150 μL of ^2H_2O, and used for NMR experiments in ^2H_2O.

NMR Experiments. To facilitate water signal suppression, all NMR experiments were performed in a 5 mm heavy-wall NMR tube. Two-dimensional (2D) ^1H NMR NOESY (Kumar et al., 1980) (relaxation delay 1.2 s, mixing time $\tau_m = 100$ and 200 ms), TOCSY (Davis & Bax, 1985) ($\tau_m = 40$ and 70 ms), and DQF-COSY (Aue et al., 1976) spectra were recorded in the phase-sensitive mode at 600 MHz (Varian Unity 600 spectrometer) at 10, 30, and 45 °C both in H_2O and in ^2H_2O, pH 3.0. The strong water signal was saturated by continuous irradiation during the relaxation delays of 2D experiments in H_2O. The spectral width was 8000 Hz, and the acquisition time was 0.256 s for all spectra. The number of complex points in the t_1 dimension was 720 for the DQF-COSY and 360 for the TOCSY and the NOESY spectra. The data were first multiplied by a shifted Gaussian weight function, then zero filled, and Fourier transformed to 8192 × 4096 complex points. Data processing took place on-line at the Sun Sparc station 10, using the spectrometer manufacturer's program VNMR. Chemical shifts were measured relative to the water resonance (4.95 ppm at 10 °C, 4.75 ppm at 30 °C, and 4.60 ppm at 45 °C). For quantitative estimation of the NH proton/solvent deuteron exchange rates (see Table S3), a series of 1D and TOCSY spectra ($\tau_m = 70$ ms) were recorded at 30 °C immediately after OSK1 being dissolved in ^2H_2O, pH 3.0. The exchange rates were calculated by exponential decay analysis of nonoverlapped peak intensity using the VNMR program.

Resonance Assignment. The resonance assignment of OSK1 was conventionally performed, according to the method of Wuthrich and Wagner (Wuthrich, 1986; Billeter et al., 1982) and using the XEASY program (Eccles et al., 1991). The assignment procedure had the following steps:

Step 1: Identification of individual resonances associated with each spin system and designation of key atom types (e.g., H^N, H^α, H^β, H^γ, etc.).

Step 2: Classification of each identified spin system with respect to one or more possible amino acid residue types.

Step 3: Identification of possible sequential relations between spin systems using interresidue NOE data.

Step 4: Unique mapping of strings of sequentially connected spin systems to segments of the amino acid sequence, thus establishing "sequence-specific assignments".

Step 5: Extension of assignments to resonances of peripheral side-chain nuclei in each spin system and determination of stereospecific assignments.

Experimental Constraints. Four types of experimental constraints were used by the DIANA program (Guntert et al., 1991a): (1) interproton distance constraints (upper and lower), (2) disulfide bridge constraints, (3) hydrogen bond constraints, and (4) torsion angle constraints determined from local structure analysis using the HABAS program (Guntert et al., 1989) and derived from the REDAC algorithm (Guntert & Wuthrich, 1991). Connectivity of cysteines and location of acceptors for hydrogen bonds involving slowly exchanging amide proton donors were determined after preliminary structure calculation.

Because cross-peaks were better visible in the 200 ms NOESY spectrum as compared to the 100 ms spectrum, we used it for complete chemical shift assignment. However, for DIANA calculation we used data on the 100 ms NOESY spectrum, due to less spin-diffusion effect. The shorter mixing time gives more accurate constraints for methylene groups and help to find stereospecific assignment.

Cross-peak integral intensities were measured in NOESY spectra using integration routines of the XEASY program. Only cross-peaks with the ratio of an integration error to integration volume <0.2 were applied for constraint list generation. Upper interproton distance constraints d_u were calculated from NOESY cross-peak volumes via the CALIBA program (Guntert et al., 1991a). Finally, we used distance constraints modified for upper limits in the following way, $d_u = 0.95d_u + 0.05d_u^2$, to account for increasing uncertainties of distance determination for small peak intensities. The CALIBA program produces typical plots of the distances between protons in calculated structures versus the corresponding upper distance constraints. The plots demonstrate that the smaller the intensity of NOE cross-peak is, the more underestimated upper constraint will be. The reason for this is quite clear and arises from the $1/r^6$ dependence of cross-peak volume versus distance and from internal mobility. To take into account these effects, we used the empirical modification formula for calibration without unnecessary loosening of short distance constraints. The number of upper distance constraints (312) was less than the number of unambiguously assigned cross-peaks (578), because some cross-peaks belonged to the protons with fixed distance between them. Very weak cross-peaks (with corresponding $d_u > 6.0$ Å) were also eliminated. For some NOEs involving prochiral centers free of stereospecific assignments, the pseudoatom constraints were utilized. There were used only upper limits ranging from 2.3 to 5.5 Å in the distance geometry algorithm.

Additional lower distance constraints were obtained by visual analysis of the absence of NOE cross-peaks between all protons of all residues. To obtain them, proton chemical shift crosses were first considered; then the crosses overlapped with cross-peaks, noisy areas, and diagonal areas and those close to diagonal were eliminated. Taking into account that intramolecular mobility might entail "disappearance" of peaks from NOESY spectra, the cross-peak absence was used as "negative" information (lower distance constraints) only if both of the protons had NOE upper distance constraints, in other words, only for protons without significant internal motion. After excluding the crosses of mobile side chains, we obtained 175 lower distance constraints. The value of lower distance constraints of 3.0 Å is quite cautious, as the smallest of NOE cross-peaks corresponds to 5.5 Å upper distance constraints. Noteworthy, first we performed structure calculation without inclusion of negative information. Its subsequent addition decreased the rmsd values for backbone heavy atoms by about 0.1 Å but caused no problems with other constraints. Thus, the negative information is helpful for the structure refinement. A total of 18 distance constraints were included in the DIANA calculation to establish the three disulfide bridges. The six distance constraints (three upper, three lower) for each disulfide bridge included an upper and lower boundary of 2.0 and 2.1 Å for $d(S^{\gamma},S^{\gamma})$, respectively, and 3.0 and 3.1 Å for $d(C^{\beta},S^{\gamma})$ across the bridge, respectively.

Twenty-four NH protons which gave detectable signals after 2 h in 1D and TOCSY spectra in ^2H_2O were supposed to be involved in hydrogen bonds. The acceptors of the hydrogen bonds were found from intra-α-helix and cross-β-strand NOE connectivities confirmed by analysis of preliminary structures (the hydrogen bonds were observed in 80−100% of the 30 structure set). Eight distance constraints were used in subsequent calculations for each hydrogen bond: four upper (3.4, 2.3, 4.6, 3.6 Å) and four lower (3.0, 1.9, 4.2, 3.2 Å) for $d(O,N)$, $d(O,H^N)$, $d(C,N)$, $d(C,H^N)$ distances, respectively, in accordance with hydrogen bond angle criteria $140° < \angle NHO < 180°$ and $130° < \angle COH < 170°$ (Yang & Honig, 1995) and distance criteria (Baker & Hubburd, 1984). That gives 192 distance constraints for 24 hydrogen bonds. After inclusion of the hydrogen bond constraints, the total number of distance constraints was 417 for upper and 280 for lower limits.

Vicinal coupling constants $^3J_{N\alpha}$ were determined from the fine structure along the ω_2 axis of the nonoverlapped NOE cross-peaks between the corresponding amide proton (at the ω_2 frequency) and any proton of neighboring residue (at the ω_1 frequency) using the INFIT program (Szypersky, 1992). A similar method was applied for measuring the $^3J_{\alpha\beta}$ constant of Ile, Thr, and Val (residues which have only one $C^{\beta}H$ proton). The fine structure of the interresidue cross-peaks in the NOESY spectrum recorded in ^2H_2O was here analyzed. The fine structure of the strongest cross-peaks between $C^{\alpha}H$ and $C^{\beta}H$ protons in the DQF-COSY spectrum recorded in ^2H_2O at 30 °C was analyzed to measure the $^3J_{\alpha\beta}$ constants for the residues containing the $C^{\beta}H_2$ group with different chemical shifts of $C^{\beta}H$ protons. An active constant was determined by measuring antiphase splitting and the passive one calculated by in-phase doublet analysis via the INFIT program.

Spatial Structure Calculation Procedure. Spatial structures were calculated by the variable target function program DIANA and further refined by constrained energy minimization in the AMBER potential of the SYBYL program (SYBYL, 1995). The calculation covered several steps:

Step 1: Generation of distance constraints using assigned resonance frequencies to interpret the NOESY spectrum in terms of "sequence-specific distance constraints". This is performed by integrating specific peak areas in the NOESY spectra with the PEAKINT subroutine of the XEASY program (Bartels et al., 1995) and subsequent calibration of the intensities into accurate upper limits for proton−proton distances with the CALIBA program.

Step 2: Analysis of local structure−local NOE constraints and $^3J_{N\alpha}$, $^3J_{\alpha\beta}$ scalar coupling constants are considered with the HABAS program to obtain φ, ψ, and χ^1 torsion angle constraints.

Step 3: Reiterative structure generation (REDAC algorithm). After several REDAC iterations (each from a random start, with the output angle constraint values used as the input for the next run), a group of structures conforming to all constraints was obtained.

Step 4: When a set of structures of reasonable quality is obtained, hydrogen−deuterium exchange data are interpreted as hydrogen bond fixed range constraints using facilities of the DIANA.

Step 5: Stereospecific assignment with the GLOMSA program (Guntert et al., 1991b). Proton stereospecific assignments in methylene and isopropyl methyl groups were determined using the GLOMSA program. The assignments were made for two α-methylene groups, twenty-three β-methylene groups, six γ-methylene groups, three δ-methylene groups, and three isopropyl groups (Table S1).

Step 6: The structures resulting from each iteration were used to resolve ambiguities during the NOESY cross-peak assignments by the ASNO program (Guntert et al., 1993). The calculation procedure is then repeated from step 1 until the assignment list is converged.

Step 7: This step was aimed at assessing the structure consistency and at confirming its topological arrangement by the procedure including energy terms, more detailed than in the DIANA. A subset of 30 "best" "DIANA" structures was selected by the criterion of small final target function values.

These structures were subjected to an 800-step constrained energy conjugate gradient minimization (Powell, 1977) using version 6.2 of the program SYBYL. Distance-dependent dielectric approximation is used for the procedure. The distribution and conformation of the charged or polar side chains in this protein are of particular interest; hence we used a very weak electrostatic term ($\epsilon = 80$) to ensure that any conformational preference among the structures was a consequence of experimental constraints and/or of steric interactions. The energy potential included pseudoenergy terms for distance and torsion angle constraints. The pseudoenergy was proportional to the second power of distance or angle violations and adjusted weight factors so that violations of 0.1 Å and 10° corresponded to 1 kcal/mol (Billeter et al., 1990). The weight factors were 100 kcal/(mol·Å^2) for distance constraints and 0.01 kcal/(mol·deg^2) for torsion angle constraints. As the commercial program SYBYL 6.2 allows only for fixed value (not a range) angle constraints, the torsional angle range constraints, used in DIANA calculations, were not included in the "SYBYL"

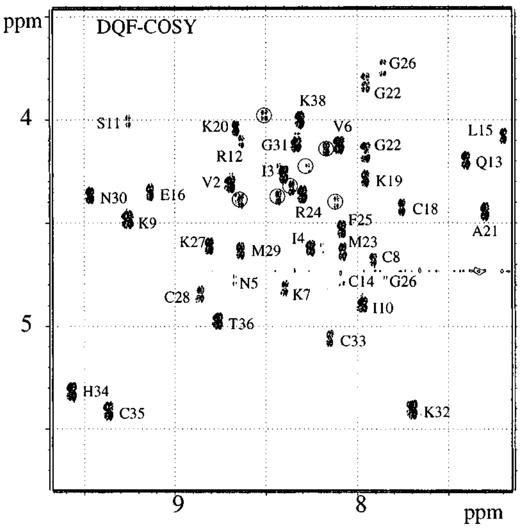

FIGURE 1: Contour plot of the fingerprint region of the DQF-COSY spectrum of OSK1 at 30 °C, pH 3.0. Assignments of NH−C$^\alpha$H cross-peaks are shown; circled peaks are due to impurities (see text).

energy minimization protocol, except for several fixed angle constraints for the well-defined χ^1 angles. After the first 200 steps of the minimization the torsion angle constraints were omitted, and the energy minimization proceeded with the distance constraint pseudoenergy term only. The use of the protocol is valid as the majority of the torsional angle ranges became narrower after energy minimization (see Figure 3) and the structures obtained well agree with experimental data (see Table 1). This result is expected for NMR structures obtained without overinterpretation of experimental data.

RESULTS

Assignment Results. The cross-peaks were assigned by identifying amino acid spin systems in DQF-COSY ("fingerprint" region, Figure 1) and the TOCSY spectra at 30 °C and then sequential resonance assignments using the *d* connectivities in the NOESY spectra. All of the 37 H^N−H$^\alpha$ cross-peaks expected for OSK1 were present in the DQF-COSY spectrum, and spin systems corresponding to the residues present in OSK1 could be identified, including aromatic moieties of Phe25 and His34. The assignment was mostly straightforward, but there were a few minor problems. Due to water presaturation, labile protons of some of side chains could not be assigned. Some peaks (e.g., H^N−H$^\alpha$ of Asn5, Cys14) were weak due to overlapping with water resonance signals. Selected spectra recorded at 10 and 45 °C provided resolution of ambiguities due to overlapping resonance signals. Besides, the assignment was somewhat difficult because of small impurities in the protein sample. A DQF-COSY spectrum recorded in H$_2$O in the fingerprint region exhibited not the expected 37 cross peaks but 44 cross peaks, 7 of which (circled in Figure 1) were very weak and located close to other strong signals. Estimated from the NOESY spectrum, the OSK1/"impurities" ratio is about 10. The impurity was not detected with mass spectrometry or HPLC methods. But this cannot rule out some sample destruction (e.g., oxidation of Met residues or deamination of Asn residues) during long NMR experiments. HPLC and mass spectroscopy analysis for technical reasons were not repeated after NMR experiments. Having failed to get assignments of the impurity peaks, we state that the cause of the impurities present in the spectra—conformational or chemical heterogeneity of the sample—remains obscure.

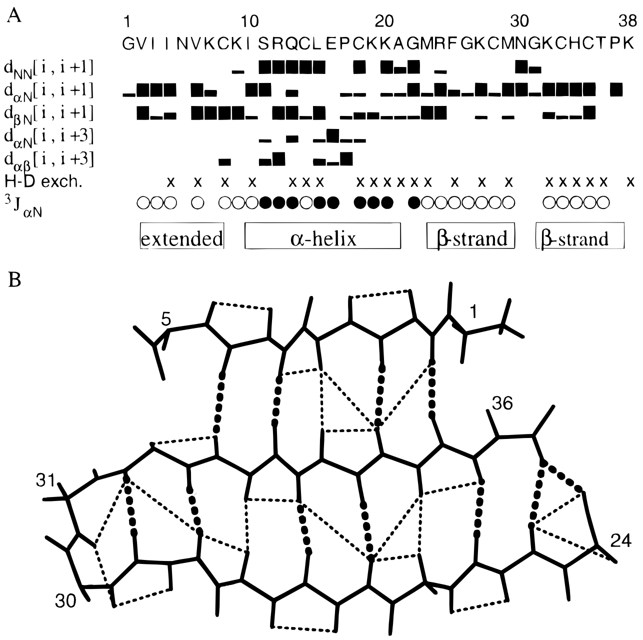

FIGURE 2: (A) Overview of NMR data defining the secondary structure of OSK1. NOE distance constraints are designated as usual: $d_{AB}(i,j)$ is the distance between the proton types A and B, respectively, located in the amino acid residues *i* and *j*, where *N*, α, and *β* denote the amide, Hα, and H*β* protons. Full-size square (■) denotes high intensity, half-size square (▄) medium intensity, and line (—) low intensity of corresponding cross-peaks in the NOESY 100 ms spectrum. $^3J_{N\alpha}$ coupling constants are (●) lower than 6 Hz and (○) greater than 8 Hz. The H−D exchange at 30 °C, pH 3.0, symbol (×) denotes times of half-exchange of amide protons >2 h. The sequence of OSK1 is shown at the top, and secondary structure elements are also indicated. (B) Sketch of the OSK1 *β*-sheet indicating the observed cross-strand NOEs (thin dashed lines) and hydrogen bonds (thick dashed lines).

Sequential NOE connectivities, hydrogen−deuterium exchange data, spin−spin coupling constant data, and secondary structure elements are summarized in Figure 2A and in Supporting Information. The resulting assignments are listed in Table S1. The assignment of ambiguously assigned or overlapped cross-peaks in NOESY spectra was performed with the ASNO program. To check the reliability of input data, we used the set of preliminary DIANA structures for semiautomatic assignment of NOESY cross-peaks. All possible variants of cross-peak assignment were listed on the basis of resonance assignment (Table S1). If the minimum distance between the two protons within the group of previously obtained structures was less than a cutoff distance of 6.5 Å, such an assignment was possible. If several possible assignments were left for a cross-peak, then the peak was assigned using line shape, the precise value of chemical shifts, and the interproton distance distribution in previously obtained structures. After updating the assignment, we repeated the peak integration, CALIBA calibration of distance constraints, and DIANA calculation. To obtain a self-consistent data set, the procedure was repeated several times.

Spin diffusion was not taken into account; it is considered to be small at the given mixing time (τ_m = 100 ms). This is vital for the stereospecific assignment of side chains having geminal protons. On the first REDAC cycle such proton pairs were treated as pseudoatoms. Subsequent REDAC cycles use the stereospecific assignment for the pairs, and more precise structures were obtained. At the final stage (after three rounds of DIANA calculations and assignment) we obtained 578 NOE peaks (198 intraresidue, 194 sequential, 28 medium range, 158 long range). Overall NOE data are summarized in the histogram showing the numbers of NOE peaks by the ranges versus sequence numbers (Figure 4) and diagonal plot (Figure S1, Supporting Information).

Local Structure Analysis. The torsion angle constraints of OSK1 were determined with the HABAS program. In the local structure analysis, 34 torsion angle constraints for φ dihedral angles were obtained from the NOE upper distance constraints and ${}^3J_{N\alpha}$,${}^3J_{\alpha\beta}$ coupling constants, using the Karplus relation (Karplus, 1963) with the Pardi coefficients (Pardi et al., 1984). Vicinal coupling constants and their errors are presented in Supporting Information (Table S2). For 27 χ^1 dihedral angles the boundaries of intervals were fixed to 60° ± 30°, −60° ± 30°, 180° ± 30° according to ${}^3J_{\alpha\beta}$ coupling constants. Besides, 37 constraints for dihedral angles ψ were generated by the HABAS program. All the constraints were used on the first REDAC iteration; the number of angle constraints then increased to the maximum possible number of 143 (35 for φ, 37 for ψ, 29 for χ^1, 21 for χ^2, 12 for χ^3, and 9 for χ^4).

Hydrogen Bonds. Qualitative analysis of *d* connectivities and investigation of conformations obtained after preliminary DIANA calculations were promoted to deduce secondary structure elements of OSK1 (Figure 2A). There is a helical region (residues Ile10−Ala21; see also Figure 7); therefore, we assumed that nine slowly exchanging amide protons in the average minimized structure formed hydrogen bonds of α-helical type (H^N−O^C: residues 14−10, 15−11, 16−12, 18−14, 19−15, 20−16, 21−17, 22−18, 23−18). The other ten amide protons form hydrogen bonds of β-sheet type, out of which six hydrogen bonds (H^N−O^C: residues 25−36, 27−34, 29−32, 32−29, 34−27, 36−25) link the two main strands (β2, β3) together and four hydrogen bonds link β3 to β1 (H^N−O^C: residues 2−35, 4−33, 33−4, 35−2). The hydrogen bond between residues Cys8 and Gly31 connects β1 and the β-turn. There are "α-helix caps" in the structure: N-cap, the side-chain carbonyl group of Gln13 forms hydrogen bonds with Lys9 and Ile10 amide protons, and C-cap, the carbonyl of Cys18 forms hydrogen bonds with Gly22 and Met23 amide protons. There is a peculiar hydrogen bond between the charged side chains of Glu16 and Arg12.

The hydrogen-acceptor partners were identified unambiguously for all NH protons of OSK1, with a slow deuterium exchange rate (with the time of half-exchange >1 h; see Figure S1). The hydrogen bonds and their characteristics are given in Supporting Information (Table S3). The average distance $d(H^N{-}O^C)$ after energy minimization was 2.23 ± 0.16 Å, and the hydrogen bond angle ∠NOH was 19.5° ± 11.2°.

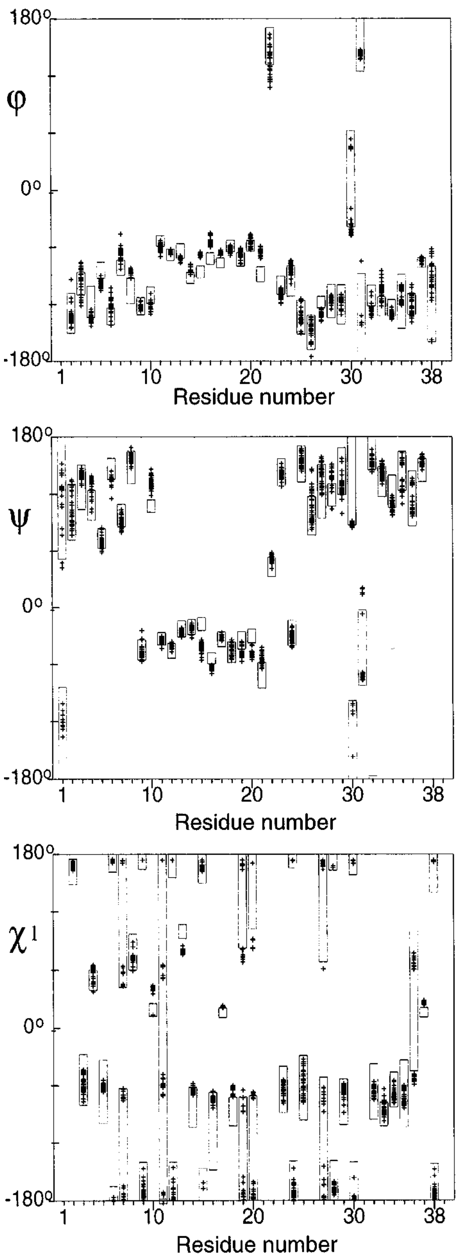

FIGURE 3: Scatter plot of the φ, ψ, χ^1 angles calculated for 30 energy-minimized SYBYL structures presented together with the corresponding angle ranges calculated from angles in the 30 best DIANA structures. Minimized conformations are shown with + symbols, whereas the ranges are shown with bounding rectangles.

Quality of the 3D Structure. The quality of the structure characterized by a scatter plot of φ, ψ, and χ^1 angles (Figure 3) and the angle and distance violations are summarized in Table 1. The table provides analysis of the 30 structures before and after energy minimization. A number of parameters characterizing the set of the structures obtained are also presented there. For example, the potential energies of the final (energy-minimized) structures are of reasonable magnitude and exhibit small structure to structure deviations. After constrained energy minimization the target function and the violations become smaller, except for some unconstrained torsion angles. As seen from Figure 3, χ^1 angles become very close to 180°, 60°, or −60°. The unconstrained φ, ψ angles are ranging wider − by 10−15° on the average. This occurs because the conformations obtained by DIANA lie between several energy minima and conformations fall to different minima during energy minimization. As follows from the mean value of the target function, the final structures agree well with NOE data. The structures have no distance violations larger than 0.2 Å and 11 dihedral violations larger than 5°. The average of the rmsd (McLachalan, 1979) between the DIANA structure and the corresponding energy-minimized structure was 0.44 ± 0.03 Å for backbone heavy atoms and 0.79 ± 0.05 Å for all heavy atoms. Pairwise rmsd values for backbone heavy atoms of the protein were 0.42

Table 1: Analysis of the 30 Best DIANA and SYBYL OSK1 structures[a]

parameter	quantity	DIANA	SYBYL
target function (Å^2)		1.32 ± 0.04	
no. of distance constraints (upper/lower)	NOE	312/175	312/175
	H-bond	96/96	96/96
	S–S bridge	9/9	9/9
no. of torsion constraints	dihedral angle	88	14
upper constraint violations (Å)	no. >0.2 Å	0 ± 0	0 ± 0
	maximum	0.19 ± 0.01	0.17 ± 0.01
	sum	1.14 ± 0.10	0.70 ± 0.06
lower constraint violations (Å)	no. >0.2 Å	0 ± 0	0 ± 0
	maximum	0.16 ± 0.02	0.09 ± 0.01
	sum	1.00 ± 0.10	0.40 ± 0.05
van der Waals constraint violations (Å)	no. >0.1 Å	8 ± 2	0 ± 0
	maximum	0.26 ± 0.03	0.0 ± 0.0
	sum	2.70 ± 0.20	0.0 ± 0.0
angle constraint violations (deg)	no. >5°	0 ± 1	10 ± 3
φ	maximum	4.1 ± 0.4	15.0 ± 2.0
	sum	25.2 ± 3.0	46.7 ± 8.0
angle constraint violations (deg)	no. >5°	0 ± 1	0 ± 1
ψ	maximum	0.6 ± 2.0	0.6 ± 2.0
	sum	0.6 ± 2.0	0.6 ± 2.0
angle constraint violations (deg)	no. >5°	0 ± 1	1 ± 2
χ^1	maximum	6.0 ± 3.3	15.0 ± 4.0
	sum	6.0 ± 3.3	15.0 ± 4.0
rmsd of residues (Å)			
1–38	backbone	0.42 ± 0.14	0.48 ± 0.13
	all heavy atoms	1.30 ± 0.20	1.34 ± 0.19
3–29, 32–37	backbone	0.34 ± 0.14	0.40 ± 0.12
	all heavy atoms	1.22 ± 0.18	1.27 ± 0.18
β-sheet: 2–6, 24–29, 32–37	backbone	0.39 ± 0.18	0.44 ± 0.15
	all heavy atoms	1.16 ± 0.22	1.19 ± 0.23
α-helix: 10–21	backbone	0.05 ± 0.02	0.16 ± 0.04
	all heavy atoms	1.02 ± 0.16	1.07 ± 0.25
⟨energy⟩ (kcal/mol)	total		60.1 ± 7.6
	dihedral		93.0 ± 2.8
	bond		16.3 ± 0.8
	angle		88.7 ± 2.8
	VDW		−186.3 ± 3.7

[a] The average values and rmsd are given for the 30 best DIANA structures before and after constrained energy minimization in SYBYL.

± 0.14 Å before and 0.48 ± 0.13 Å after energy minimization.

According to the Ramachandran plot of the 30 structures the majority of φ, ψ angles are in favorable regions; only Gly22, Gly31, and Asn30 residues are outside (Figure S2, Supporting Information). By analysis of φ, ψ, χ^1 angle distribution (Figure 3) and residues' local rmsd (Figure S3, Supporting Information) it becomes quite clear that the backbone structure is well-defined. The N- and C-ends of the protein are mobile. The set of structures obtained after SYBYL refinement may reflect dynamic behavior of the protein in solution and may be explained by the incomplete constraint list used for the structure calculation and minimization procedures.

Backbone Structure. The secondary structure of OSK1 was delineated by a well-assessed procedure [see Wuthrich (1986)] based on analysis of the sequential and nonsequential NOEs and of the $^3J_{N\alpha}$ coupling constants. Additional support was provided by hydrogen–deuterium exchange data. Four distinct regions with regular structure emerge in OSK1 (Figure 2A). First, the presence of a short α-helix (see below) is supported by the existing sequential d_{NN} connectivities associated with the observation of $d_{\alpha N}(i,i+3)$ and $d_{\alpha\beta}(i,i+3)$ and of $^3J_{N\alpha}$ coupling constants being smaller than 6 Hz. Second, our data (Figure 2) indicate that an antiparallel β-sheet (see below) is characterized by the sequential $d_{\alpha N}$ and large $^3J_{N\alpha}$ coupling constants. It presents a typical pattern of long-range $d_{\alpha\alpha}$, d_{NN}, and $d_{\alpha N}$ connectivities (Figure 2A). The Asn30–Gly31 part joins the two strands by a turn (see below). Besides, the position of hydrogen bonds characterizes the precise location of the β-sheet. Residues Gly1–Lys9 are in the "extended" conformation, thus meaning that the chain turns gradually, rather than sharply. The respective spatial arrangement of the α-helix and the β-sheet in the calculated three-dimensional structure reflects long-range NOEs between the helix and β2 strand (24–29) as well as long-range NOEs between the extended fragment β1 (1–8) and β3 part (30–37) of the β-sheet (Figure 2B). So, the structure of OSK1 is of the α/β-protein type. Figure 7 highlights the most interesting structure elements of OSK1.

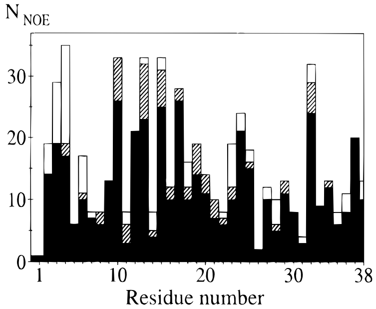

FIGURE 4: Histogram of numbers of NOE contacts for residues by ranges: filled, intraresidue and sequential contacts; dashed, medium-range contacts (2–5 residues apart); open, long-range contacts (>5 residues apart).

(A) Helix. The helix Ile10–Ala21 is amphipathic. It contains one proline residue (Pro17) which distorts the α-helical structure. The proline residue introduces a kink in the helix axis that results in bending of about 30° from the helix axis. Such a proline bend is already described (Piela et al., 1987). The bend is in accordance with the Cys14 $^3J_{N\alpha}$-coupling constant value of 9.0 Hz. It is very typical of all scorpion toxins playing an important role in the family biological functioning. Apart from the kink, the helix type is a canonical right-handed α-helix, with φ, ψ angles ranging from −50° to −80° and −10° to −70°, respectively (Figure 3).

(B) β-Sheet. The β-sheet of OSK1 is constituted of three strands (Figures 2, 5, 7): the extended part, residues Val2–Val6 (β1), and the main part, residues Met23–Met29 (β2) and Lys32–Lys38 (β3). There is a bulge in the β-sheet involving residues Met23, Arg24, and Pro37, due to proline steric intervention. The β-sheet is well-defined (backbone rmsd value of 0.39 ± 0.18 Å) (Table 1). As far as β-sheet twist is concerned, we have a right-handed moderately twisted antiparallel β-sheet, packed against the α-helix. The twist angle is about 30°. The angle corresponds to the rotation angle per repeating dipeptide unit around the strand's principal axis [for definition see Yang and Honig (1995)].

(C) Turn. The two main strands of the β-sheet are linked to each other by the β-turn, formed by Asn30 and Gly31. This turn appears to be a very flexible area as exhibited by high global rmsd values of the backbone atoms of Asn30 and Gly31 which reach 0.67 ± 0.49 Å. The turn possesses the hydrogen bond between i and i+3 residues. Characteristic NOE connectivity was observed between the two amide protons of residues i+1 and i+2, consistent with a type II or II′ (mirror conformation of II) turn. But the intensity of

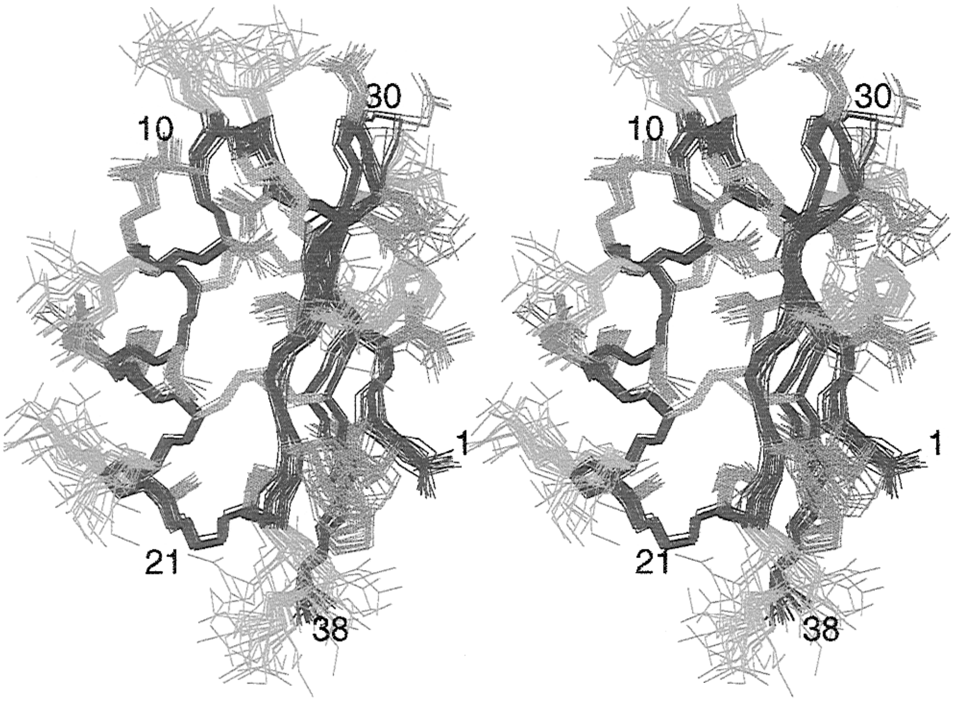

FIGURE 5: Stereoview of superposition of 30 SYBYL-refined structures. All heavy atoms are shown: backbone atoms are colored in black, positively charged side chains in cyan blue, negatively charged in red, neutral in green, and disulfide bridges forming a hydrophobic core in yellow-orange.

Table 2: Conformations of Disulfide Bridges

S_i-S_j bridge	% of structures	$\langle\chi^1{}_i\rangle$	$\langle\chi^2{}_i\rangle$	$\langle\chi^{ss}{}_{ij}\rangle$	$\langle\chi^2{}_j\rangle$	$\langle\chi^1{}_j\rangle$
Cys8−Cys28	93	76.5 ± 5.5	−147.8 ± 3.8	−95.3 ± 4.4	−165.7 ± 4.8	−167.8 ± 5.4
	7		90.9 ± 0.4	88.4 ± 0.2	65.5 ± 1.1	
Cys14−Cys33	90	−64.3 ± 2.7	169.6 ± 1.8	79.1 ± 2.8	175.4 ± 1.9	−82.9 ± 6.6
	10		−81.7 ± 2.4	−74.9 ± 1.8	−68.4 ± 2.6	
Cys18−Cys35	50	−64.5 ± 4.6	−162.6 ± 2.0	77.5 ± 1.8	174.2 ± 3.7	−68.7 ± 7.7
	50		−47.4 ± 3.4	−75.5 ± 3.4	−49.0 ± 7.0	

this NOE is weak and corresponds to 4 Å distance between the two amide protons. The distance should be far shorter (2.6 Å) in the canonical II or II′ β-turn. The decrease of the NOE intensity occurs due to the dynamical behavior of the turn. Analysis of φ, ψ angles (Figure 3) shows that only two conformations (φ_{30}, $\psi_{30} = -60°$, 100° and φ_{31}, $\psi_{31} = 125°$, $-60°$) and φ_{30}, $\psi_{30} = 60°$, $-100°$ and φ_{31}, $\psi_{31} = -125°$, 60°) are found among the 30 structures of OSK1. The two conformations are compatible with the canonical type II and type II′ β-turn (Ghelis & Yon, 1982), respectively.

Side Chains. A substantial part of the OSK1 solvent-exposed surface is positively charged due to a large number (7) of lysine side chains. This suggests that OSK1 may interact with negatively charged molecules.

In the set of OSK1 structures, as seen from χ^1 angle plot of Figure 3, the side-chain conformations of Lys7, Ser11, Lys19, Lys20, Lys27, and Thr36 are uncertain. These uncertainties might arise due to mobility or coincidental equality of chemical shifts of geminal β-protons for the residues (Table S1). Mobility of several nonpolar side chains of the molecule is restricted by hydrophobic interactions between the α-helix and β-sheet. The side chain of Gln13 forms a hydrogen bond with both Lys9 and Ile10 amide protons. The side chains of Arg12 and Glu16 form the salt bridge stabilizing the middle turn of the helix. Their contact is confirmed by the slowly exchanging amide proton of the arginine side chain. The side chain of Arg24 and C-end carbonyl of Lys38 may also form a salt bridge, but we could not confirm it. It is worth noting that DIANA calculations did not determine precisely some side-chain conformations, whereas after SYBYL minimization angles χ^1 became centered around the conformations preferred energetically (Figure 3).

No free SH groups were found in OSK1. Thus three disulfide bridges were expected. Analysis of S−S distance distribution after preliminary DIANA calculations provides the only possibility for the formation of three disulfide bridges: Cys8−Cys28, Cys14−Cys33, and Cys18−Cys35. These bridges are of much importance for the OSK1 structure. Two of the bridges connect the α-helix and β3-strand and stabilize their relative positioning; the third one (8−28) connects the extended fragment and the β-sheet together. The conformations of χ^1 angles of the disulfide bridges are defined (Table 2) due to the NOE and $^3J_{N\alpha}$, $^3J_{\alpha\beta}$ coupling data. There are two sets of χ^2 and χ^{ss} angles for each bridge. This dispersion can occur either due to insufficient experimental data or due to the internal flexibility of the disulfide bridges.

DISCUSSION

We obtained the spatial structure of OSK1 in aqueous solution using a distance geometry approach, based on accurately determined upper and lower distance constraints and restrained energy minimization with the SYBYL AM-

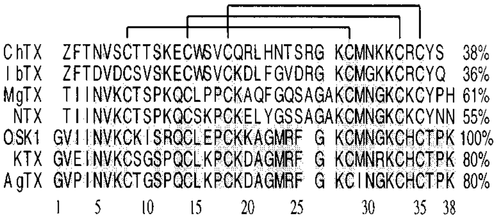

```
ChTX   ZFTNVSCTTSKECWSVCQRLHNTSRG KCMNKKCRCYS  38%
IbTX   ZFTDVDCSVSKECWSVCKDLFGVDRG KCMGKKCRCYQ  36%
MgTX   TIINVKCTSPKQCLPPCKAQFGQSAGAKCMNGKCKCYPH 61%
 NTX   TIINVKCTSPKQCSKPCKELYGSSAGAKCMNGKCKCYNN 55%
OSK1  GVIINVKCKISRQCLEPCKKAGMRF  G KCMNGKCHCTPK 100%
 KTX  GVEINVKCSGSPQCLKPCKDAGMRF  G KCMNRKCHCTPK 80%
AgTX  GVPINVKCTGSPQCLKPCKDAGMRF  G KCINGKCHCTPK 80%
      1   5    10   15   20   25     30   35 38
```

FIGURE 6: Sequence alignment of OSK1 and other scorpion toxins. The alignment is numbered according to the OSK1 sequence; disulfide bridges are shown in connecting lines, homologous residues are shaded, and the percentage of homology to the OSK1 sequence is indicated on the right.

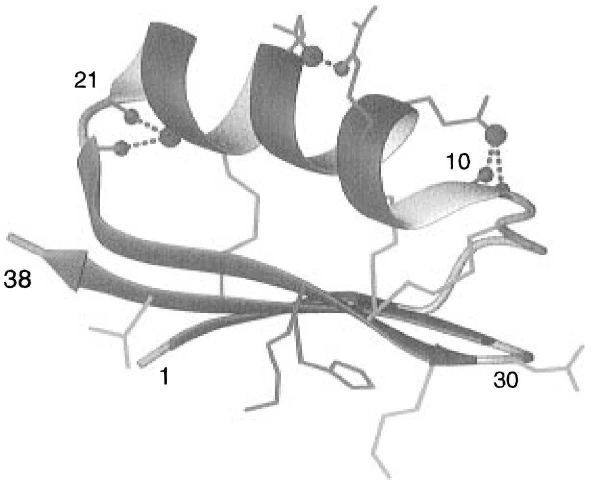

FIGURE 7: Schematic representation of the OSK1 structure with the active site oriented downward showing the helix (red-yellow spiral), three-stranded β-sheet (blue tapes), three disulfide bridge arrangement (yellow-orange lines), two connecting loops (gray tubes), N-cap and C-cap of the helix (cap atoms: O, red sphere; H^N, blue sphere) with their hydrogen bonds shown in gray dash lines, and atoms of the salt bridge Arg12−Glu16 shown by spheres. Side chains of critical residues (36, 27, 34, 29, 30) are shown in color (neutral, cyan; positive, blue). C-End, N-end, and Ile10, Ala21, and Asn30 residue numbers are printed also. (The picture was generated with the MOLMOL program.)

BER potential. The OSK1 adopts an α/β-fold primarily composed of the three-stranded moderately twisted β-sheet, promoting close contacts with a slightly bent α-helical fragment. The C- and N-end and the β-turn area as well as some side chains are very mobile.

On the basis of the toxin fine spatial structure, sequence alignment of the homologues, and mutagenesis analysis as well as comparison of the scorpion toxin family specificity and function, we shall further delineate some differences significant for exhibiting the specificity.

The scorpion toxin family proteins differ from each other in the variety of specificities and selectivities (see the introduction). We performed thorough comparison of the spatial structure of the OSK1 and of the homologues. When comparing the mutation analysis results, one should align the toxin sequences. In Figure 6 they are aligned according to the OSK1 sequence. The sequences have many (6−8) positively charged residues and a few (1−2) negatively charged residues, which is significant as the toxins interact with negatively charged surfaces (Anderson et al., 1988). The spatial structure of OSK1 is rather close to those of AgTX, ChTX, NTX, and MgTX. The general fold is of the same topology. The general appearance of the toxins is also very similar. Their α-helices are bent in the middle and their β-sheets are moderately right-hand twisted. However, detailed examination of the toxin structures reveals some structural differences resulting in diverse specificity. We shall discuss here the differences and their importance for the function.

Of interesting findings in the OSK1 structure we consider the presence of "N-cap" and "C-cap" formed by two bifurcated hydrogen bonds: at the N-end of the α-helix the side-chain carbonyl of Gln13 forms hydrogen bonds to amide protons of Lys9 and Ile10, and at the C-end the carbonyl of Cys18 forms hydrogen bonds to Gly22 and Met23 amide protons. This finding is confirmed by slow exchange rates for the amide protons and the DIANA calculations. It is worth noting that Gln13 is conserved in the family (Figure 6). The residue is important due to its function in the N-cap, fixing the end of the α-helix. It is mutated to Glu13 only in ChTX and IbTX, which obviously does not violate the cap formation. One can propose a mutation at this place for a residue without the side-chain carbonyl group with possible resulting violation of folding and a decrease in the toxin specific activity. The hydrogen-bonded salt bridge between the charged side chains of Arg12 and Glu16 (residues i, $i+4$) is another interesting feature of the structure. The bridge is important for the structure, as it additionally stabilizes the α-helix in its middle part. This finding is confirmed by the following facts: χ^1 angles of Arg12 and Glu16 are fixed (Figure 3), amide proton $H^{N\epsilon}$ of the Arg12 side chain has a low exchange rate, and NOEs corresponding combination is observed. This hydrogen bond was not reported for the other toxins, but it can be located at a different place on the helix. For example, in NTX there could be a salt bridge between residues Lys16 and Glu20 and in KTX and AgTX between Lys16 and Asp20. In MgTX a hydrophobic interaction was observed between side chains of Pro16 and Ala20. Apart from the helix structure fixing, such bridges can play a certain role in the toxin specificity. For example, such a bridge can compensate for a kink in the α-helix due to proline residues. The kink can drive the twist angle of the positively charged β-sheet surface of toxins that fits to the receptor surface. Interestingly, whenever there are prolines in the α-helix region, the formation of such a bridge appears to be possible (Figure 6): for OSK1, it is copresence of Pro17 and the Arg12−Glu16 bridge; for KTX and AgTX, Pro12, Pro17, and Lys16−Asp20; for NTX, Pro11, Pro17, and Lys16−Glu20; for MgTX, Pro11, Pro16, Pro17, and a hydrophobic interaction between Pro16 and Ala20; and in the extreme case of ChTX and IbTX, no proline, and there is no need for a stabilizing bridge.

The flexible β-turn formed by conservative Asn30 and Gly31 residues is very important for the toxin activity, as it is involved in the close interaction with the receptor (Goldstein et al., 1994). The type of the β-turn for most toxins is not established, except for OSK1 and NTX. For OSK1 it is type II, II′, whereas for NTX it is type I, I′ (Dauplas et al., 1996). The difference in the type of β-turn does not immediately arise from amino acid sequences of NTX and OSK1; for both of the toxins the residues from 27 to 33 are the same (Figure 6). The difference might be explained by mutation of spatially proximate residues. In NTX there are insertions of two alanines on both sides of the conserved residue Gly26. The insertion leads to rearrangement of the disulfide bridge (8−28 in OSK1) connecting the β-sheet and the N-end of the α-helix. MgTX also has such an alanine insertion. This difference might be another source for the specificity among the scorpion toxin family. NTX and MgTX inhibit the delayed rectifier voltage-dependent K^+ channel with little effect on Ca^{2+}-activated K^+ channels, whereas OSK1 action is vice versa.

We continue with function−structure mapping. Analysis of the effect of a large number of ChTX mutations on its interaction with the Shaker channel provided elucidation of the interaction surface of the toxin (Goldstein et al., 1994). The surface is composed of 5 residues that are *critical* to the interaction, Lys27, Arg34, Met29, Tyr36, and Asn30; 8 residues that are *influential*, PyroGlu2, Phe3, Ser11, Thr24, Ser25, Arg26, Lys31, and Ser37; 17 *indifferent* residues, Thr4, Asn5, Val6, Ser7, Thr9, Thr10, Lys12, Glu13, Trp15, Ser16, Val17, Gln19, Arg20, Leu21, His22, Asn23, Lys32; and 7 residues (including 6 cysteines) did not mutate. According to Goldstein et al. (1994), the pair Thr9, Thr10 determines the specificity of the ChTX interaction with the Shaker channel. Wild-type ChTX has high affinity for high-conductance Ca^{2+}-activated K^+ channels and medium affinity for Shaker channels. Double mutant T9S+T10G of ChTX binds to the Shaker channel 7-fold more tightly than the wild-type ChTX does. Thr9 and Thr10 in OSK1 are substituted for bulkier residues Lys9 and Ile10, which may account for the different specificity of OSK1 to the receptor (affinity for small-conductance Ca^{2+}-activated K^+ channels etc.).

The importance of toxin charged side chains for blocking of the negatively charged receptor cannot be overestimated. Therefore, we shall consider the involvement of the side chains in the interaction. The main role in the binding belongs to the positively charged side chain of Lys27 inserted into the "hole" in the middle of the receptor pore (Goldstein, 1994). The K^+ channels were shown to have negatively charged residues near their pore. According to Figure 6, some of the residues, critical for binding of ChTX to the Shaker channel, are conserved within the family. These include the very important Lys27 residue and two β-turn residues−Asn30 and Met29 (in AgTX Met29 is replaced by the similar residue Ile29; as it follows from the ChTX mutation analysis such mutation is indivisible). Two other critical residues, Arg34 and Tyr36 of ChTX, are not conserved in the family, which is why their replacement might be significant for the toxin specificity. Figure 6 presents two groups of toxins differing in the residues in positions 34 and 36. The first group embraces ChTX, NTX, and MgTX with Lys34 and Tyr36 (except for ChTX having Arg34, but the mutation of Arg34 to Lys34 in ChTX almost does not change its specificity to the Shaker channel). The second group covers OSK1, KTX, and AgTX with His34 and Thr36. We suggest that one group is more specific to the Ca^{2+}-activated K^+ channels, whereas the other shows better binding to the voltage-dependent K^+ channels. Interestingly, in the case of OSK1, KTX, and AgTX unfavorable Pro17 is situated in the middle of the α-helix. Its side chain has a hydrophobic interaction with the Ala21 side chain.

We revealed that the side chain of Thr36 in OSK1 is mobile and has two conformations (Figure 3), whereas for His34 angle χ^1 was fixed, but χ^2 covered an almost 180° range. The following residues were found to have mobile side chains−Lys7, Ser11, Lys19, Lys20, Lys27, His34, and Thr36−and mobile main chains−Gly1, Asn30, Gly31, and Lys38. Moreover, there is an essential correlation with residue importance (i.e., if it is critical or significant) and its mobility: Lys27, His34, Thr36, Asn30, Gly31, Gly1, Ser11, and Lys38 are important and mobile. All critical residues are mobile (Met29 is located in the flexible turn). Hence, we suggest that certain toxin conformations are selected upon binding to the receptor. Even though upon such binding the configurational entropy of the ligand decreases, the loss could be compensated by origination of new low-frequency collective motions in the complex [e.g., see Chou (1988)] and by removal of immobilized water from contact surfaces of the ligand and the receptor. Besides, in the "well-fitted" complex a significant gain in binding affinity is expected due to the enthalpy term. Scorpion toxins are known to bind to different receptors; i.e., contact surfaces of the receptors are different. Therefore, a closer fit to different receptor surfaces seems possible for a ligand with mobile side chains, whereas the ligand-fixed conformation assumes the receptor surface to be very particular.

The spatial structure of OSK1 has minor but important differences from the other scorpion toxins, which results in their different biological functioning. The structure precisely determined is of considerable interest to our future studies on scorpion toxin family specificity and structure−function relationships and to rational design of highly specific toxins.

ACKNOWLEDGMENT

The authors thank Prof. K. Wuthrich for providing the programs DIANA and MOLMOL.

SUPPORTING INFORMATION AVAILABLE

Figure S1 with a diagonal plot of NOE/H-bond information, Figure S2 with a Ramachandran φ, ψ plot for all residues in the 30 energy-refined structures of OSK1, Figure S3 with plots of residues' local rmsd, Table S1 with chemical shifts, Table S2 with spin−spin coupling constants, and Table S3 with hydrogen bonds data (7 pages). Ordering information is given on any current masthead page.

REFERENCES

Anderson, C., MacKinnon, R., Smith, C., & Miller, C. (1988) *J. Gen. Physiol. 91*, 317−333.

Aue, W. P., Bartholdi, E., & Ernst, R. R. (1976) *J. Chem. Phys. 64*, 2229−2246.

Baker, E. N., & Hubburd, R. E. (1984) *Prog. Biophys. Mol. Biol. 44*, 97−179.

Bartels, C., Xia, T. H., Guntert, P., Billeter, M., & Wuthrich, K. (1995) *J. Biomol. NMR* (in press).

Billeter, M., Braun, W., & Wuthrich, K. (1982) *J. Mol. Biol. 155*, 321−346.

Billeter, M., Shaumann, T., Braun, W., & Wuthrich, K. (1990) *Biopolymers 29*, 695−706.

Blatz, A. L. (1987) *Trends Neurosci. 10*, 463−467.

Bontems, F., Gilquin, B., Roumestand, C., Menez, A., & Toma, F. (1991) *Science 254*, 1521−1524.

Bontems, F., Gilquin, B., Roumestand, C., Menez, A., & Toma, F. (1992) *Biochemistry 31*, 7756−7764.

Chou, K. C. (1988) *Biophys. Chem. 30*, 3−48.

Dauplas, M., Gilquin, B., Possani, L. D., Gurrola-Briones, G., Roumestand, C., & Menez, A. (1996) in *Protein Data Bank*, entry code 1SXM.

Davis, D. G., & Bax, A. (1985) *J. Am. Chem. Soc. 107*, 2820−2821.

Eccles, C., Xia, T. H., Billeter, M., & Wuthrich, K. (1991) *J. Biomol. NMR 1*, 111−130.

Fernandez, I., Romi, R., Szendeffy, S., Martin-Eauclair, M. F., Rochat, H., Van Rietschoten, J., Pons, M., & Giralt, E. (1994) *Biochemistry 33*, 14256−14263.

Ghelis, C., & Yon, J. (1982) in *Protein Folding*, pp 52−55, Academic Press, San Diego, CA.

Goldstein, S. A. N., Pheasant, D. J., & Miller, C. (1994) *Neuron 12*, 1377−1388.

Grishin, E. V., Korolkova,Y. V., Kozlov, S. A., Lipkin, A. V., Nosyreva, E. D., Pluzhnikov, K. A., Sukhanov, S. V., & Volkova, T. M (1996) *Pure Appl. Chem. 68*, 2105−2109.

Guntert, P., & Wuthrich, K. (1991) *J. Mol. Biol. 1*, 447−456.

Guntert, P., Braun, W., Billeter, M., & Wuthrich, K. (1989) *J. Am. Chem. Soc. 111*, 3997−4004.

Guntert, P., Braun, W., & Wuthrich, K. (1991a) *J. Mol. Biol. 217*, 517−530.

Guntert, P., Qian, Y. Q., Otting, G., Muller, M., Gehring, W., & Wuthrich, K. (1991b) *J. Mol. Biol. 217*, 531−540.

Guntert, P., Berndt, K. D., & Wuthrich, K. (1993) *J. Biomol. NMR 3*, 601−606.

Johnson, B. A., & Sugg, E. E. (1992) *Biochemistry 31*, 8151−8159.

Johnson, B. A., Stevens, S. P., & Williamson, J. M. (1994) *Biochemistry 33*, 8146−8159.

Karplus, M. (1963) *J. Am. Chem. Soc. 85*, 2870−2871.

Kreizel, A. M., Kasibhatla, C., Hidalgo, P., Mackinnon, R., & Wagner, G. (1995) in *Protein Data Bank*, entry code 1AGT.

Kumar, A., Ernst, R. R., & Wuthrich, K. (1980) *Biochem. Biophys. Res. Commun. 95*, 1−6.

Leonard, R. J., Garcia, M. L., Slauther, R. S., & Reuben, J. P. (1992) *Proc. Natl. Acad. Sci. U.S.A. 89*, 10094−10098.

McLachalan, A. D. (1979) *J. Mol. Biol. 128*, 49−79.

Meuner, S., Bernassau, J. M., Sabatier, J. M., Martin-Eauclair, M. F., Rietschoten, J. V., Cambillau, C., & Darbon, H. (1993) *Biochemistry 32*, 11969−11976.

Pardi, A., Billeter, M., & Wuthrich, K. (1984) *J. Mol. Biol. 180*, 741−751.

Piela, L., Nemethy, G., & Scheraga, H. A. (1987) *Biopolymers 26*, 1587−1600.

Powell, M. J. D. (1977) *Math. Program. 12*, 241−254.

Reinhart, P. H. (1989) *Neuron 2*, 1031−1041.

SYBYL version 6.2 (1995) *Molecular modelling software*, TRIPOS Associates, Inc.

Szypersky S. (1992) *J. Biomol. NMR 2*, 432−440.

Valdivia, H. H., Smith, A. S., Martin, B. M., Coronado, R., & Possani, L. D. (1988) *FEBS Lett. 226*, 280−284.

Vazquez, J. (1990) *J. Biol. Chem. 265*, 15564−15571.

Vita, C., Roumestand, C., Toma, F., & Menez, A. (1995) *Proc. Natl. Acad. Sci. U.S.A. 92*, 6404−6408.

Wuthrich, K. (1986) in *NMR of Proteins and Nucleic Acids*, John Wiley & Sons, New York, NY.

Yang, A. S., & Honig, B. (1995) *J. Mol. Biol. 252*, 366−376.

BI9614390